

Angular dependent micro-resonator ESR characterization of a locally doped $\text{Gd}^{3+}:\text{Al}_2\text{O}_3$ system

I. S. Wisby,^{1,2} S. E. de Graaf,¹ R. Gwilliam,³ A. Adamyan,⁴
S. E. Kubatkin,⁴ P. J. Meeson,² A. Ya. Tzalenchuk,^{1,2} and T. Lindström¹

¹*National Physical Laboratory, Hampton Road Teddington, TW11 0LW, UK*

²*Royal Holloway, University of London, Egham, TW20 0EX, UK*

³*Advanced Technology Institute, Faculty of Electronics and Physical Sciences,
University of Surrey, Guildford, Surrey, GU2 7XH, UK*

⁴*Department of Microtechnology and Nanoscience, MC2,
Chalmers University of Technology, SE-41296 Gothenburg, Sweden*

(Dated: November 12, 2018)

Interfacing rare-earth doped crystals with superconducting circuit architectures provides an attractive platform for quantum memory and transducer devices. Here we present the detailed characterization of such a hybrid system: a locally implanted rare-earth Gd^{3+} in Al_2O_3 spin system coupled to a superconducting micro-resonator.

We investigate the properties of the implanted spin system through angular dependent micro-resonator electron spin resonance (micro-ESR) spectroscopy. We find, despite the high energy near-surface implantation, the resulting micro-ESR spectra to be in excellent agreement with the modelled Hamiltonian, supporting the integration of dopant ions into their relevant lattice sites whilst maintaining crystalline symmetries. Furthermore, we observe clear contributions from individual microwave field components of our micro-resonator, emphasising the need for controllable local implantation.

A reliable and scalable quantum information architecture requires a quantum memory [1]. A promising route to realizing such a device lies in a hybrid approach, where the unique and desirable properties of a variety of independent physical systems are exploited in conjunction[2]. There has been particular interest in combining superconducting circuits with other two-level systems (TLS) including cold atoms and ions [3–5], two-level defects [6, 7], molecules [8, 9] and spin ensembles [10–13] - each of which are uniquely suited to individual operation parameters.

One system of particular interest for microwave quantum memory applications are rare earth (RE) ions doped into crystals [7, 14–19]. These ion species are particularly promising as their inner $4f$ optical electronic transitions have very long coherence times [20]. Specific RE ions also have the potential for photon conversion between optical and microwave frequency bands for quantum transducer applications [17, 21].

For now, focus has turned to the requirement for a controllable and scalable infrastructure [1], leading to the development of local ion implantation [22, 23] or specialist focused ion beam [24] techniques for precision dopant control which is not otherwise achievable from a growth process alone. With this in mind, we have previously demonstrated a local doping technique utilizing a hard nitride mask to create a locally defined RE spin system, whereby coupling to a superconducting micro-resonator was demonstrated on the order of 3 MHz [22]. While the potential of such a device was evident, it was ascertained from our work, along with that of others [25], that when employing such implantation techniques coupling strengths are limited by excessive line-width broadening on the scale of $\approx 50 - 100$ MHz.

It is therefore imperative that we study these locally doped crystals and their structure in detail, on the scale at which coupling is mediated. This is, however, challenging due to the nature of local-implantation, where the number of dopant ions is considerably lower (of order 10^{11}) than in grown, doped crystals. Whilst techniques such as conventional electron spin resonance (ESR), photoluminescence, x-ray photoelectron spectroscopy and secondary ion mass spectroscopy lack the sensitivity required to obtain measurements of such a small spin ensembles, ultra-sensitive microwave spectroscopy at milli-kelvin temperatures has shown more promise [18, 22, 26, 27].

In this work, we explore the properties of an implanted gadolinium (Gd^{3+}) in Al_2O_3 spin system through angular dependent micro-resonator ESR (micro-ESR) spectroscopy. We find the measured angular dependent micro-ESR spectra to be in excellent agreement with the modelled Hamiltonian. This supports the conclusion that the dopant ions are well integrated into their relevant lattice sites and that crystalline symmetries are maintained. Furthermore, we observe clear contributions from individual microwave field components of our micro-resonator device, emphasising the need for controllable local implantation.

The data shown in this work is obtained using a sample consisting of seven, frequency multiplexed, inductively coupled, NbN superconducting micro-resonators fabricated atop a systematically implanted Gd^{3+} rare-earth ion ensemble.

The focus of this work is on a lumped element (LE) resonator of centre frequency $\omega_r/2\pi = 3.352$ GHz which sits on a R-cut Al_2O_3 substrate with locally implanted Gd^{3+} in a 100×250 μm area (Fig. 1a). The number of

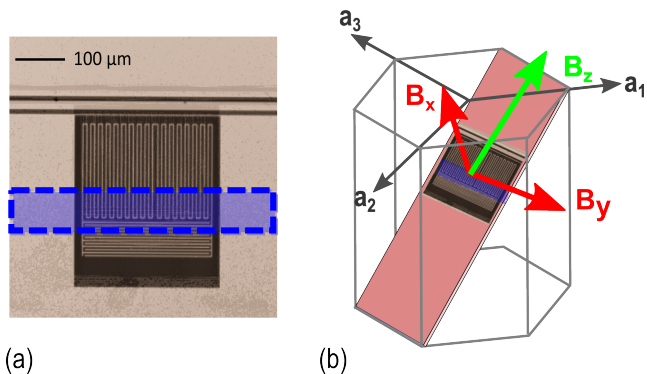


FIG. 1. (a) An optical image of the LE resonator used in this work. The device is inductively coupled to the transmission line and sits atop a region implanted with Gd^{3+} ions, which is highlighted for clarity with false colouring. (b) The sample is mounted and magnetic field aligned such that the R-plane is parallel to the magnet B_z and B_y axes.

spins beneath the resonator is $N \approx 10^{11}$.

The samples are fabricated utilizing a silicon-nitride mask technique which is detailed extensively in previous work [22] and is briefly outlined as follows:

The local implantation process comprises initial deposition of alignment markers which are evaporated atop a commercial R-cut Al_2O_3 wafer. A SiN mask is next created to act as a stopping barrier for the incident ions during the ion implantation process, and is patterned such that only μm -size exposed windows will be subject to implantation. The depth profile of the implanted ensemble can be altered by tuning the implantation energy and dose parameters. In our case, $^{160}\text{Gd}^{3+}$ is implanted at room temperature at a dose of 1×10^{14} ions/ cm^2 and at an energy of 900 keV, giving a concentration profile with peak implantation depth of 170 nm and full-width-half-maximum = 77 nm.

The contaminated SiN mask is then removed and the implanted substrate annealed at 980°C for 1 hour in order to remove lattice defects and restore surface crystalline quality. A NbN thin film is then deposited and resonator devices are patterned with standard e-beam lithography techniques whilst ensuring alignment to the implanted regions.

The micro-ESR experiment is performed at mK temperatures in a dilution refrigerator fitted with a vector magnet. The system is equipped with heavily attenuated microwave lines and a low noise cryogenic amplifier.

The magnetic field axis is aligned such that the superconducting plane is parallel to the applied magnetic field B_z and B_y axes, as shown in Fig. 1b. Initial characterization of the micro-resonator is performed using a vector network analyser (VNA) at $T \approx 10$ mK, with a power in the resonator of ≈ 3 pW. From S_{21} measurement we extract internal and coupled quality factors of $Q_i = 3.3 \times 10^5$, $Q_c = 3.8 \times 10^4$ respectively - giving a zero field resonator dissipation rate $\kappa/2\pi = 0.13$ MHz.

We next perform angular absorption spectroscopy at

an enhanced $T = 250$ mK in order to observe higher order transitions. An external static magnetic field (B_0) is applied in the R-plane of the Al_2O_3 substrate and is rotated in this plane a full 360° in 4° intervals. We assume nominal 0° rotation where $B_0 = B_z$. For each B_0 rotation, we apply microwaves on resonance with our micro-resonator and step B_0 from 0 – 120 mT, tuning the spin ensemble Zeeman transitions into resonance at spin frequency degeneracies. At each B_0 step the local S_{21} minima is tracked and $Q_m = Q_i + Q_c$ is extracted from S_{21} measurements.

The residual loss tangent due to the ions ($\tan \delta_{ions}$) is extracted from each absorption spectroscopy trace via numerical fitting of the total measured loss tangent: $\tan \delta_m = 1/Q_m = \tan \delta_c + \tan \delta_{int}$, where $\tan \delta_c$ is due to coupling to the transmission line. $\tan \delta_{int}$ are intrinsic losses attributable to a summation of the dielectric, magnetic field and losses due to the ions. From $\tan \delta_{int}$ we extract the field dependent loss by subtracting the zero-field losses. The remaining $\tan \delta_B$ includes loss due to the ions, while other magnetic field induced losses are assumed to be negligible, such that $\tan \delta_B = \tan \delta_{ions}$.

An example of a single absorption spectroscopy trace for a B_0 rotation of 5° is shown in Fig. 2a, where ESR's are observed as an additional absorption mechanism for the microwave photons. The total angular dependent ESR spectra is shown in Fig. 2b as an intensity plot, where we have applied an edge detection filter to enhance weaker transitions such that areas of high contrast correspond to ESR's.

In order to understand our results, we next examine the ESR spectra using the EASYSPIN [28] software package to model the angular dependence of the $\text{Gd}^{3+}:\text{Al}_2\text{O}_3$ system within our experimental parameters. In order to achieve this we first consider the spin system and experimental parameters independently.

The spin system is described by the Hamiltonian

$$\mathcal{H} = g\mu_b B \cdot S + B_2^0 O_2^0 + B_4^0 O_4^0 + B_6^0 O_6^0 + B_4^3 O_4^3 + B_6^3 O_6^3 + B_6^6 O_6^6,$$

where O_k^q are hermitian spin operators and B_k^q coefficients are real parameters. It is customary to redefine these B_k^q operators in the spin Hamiltonian as:

$$b_2^0 = 3B_2^0 \quad b_4^0 = 60B_4^0 \quad b_6^0 = 1260B_6^0 \\ b_4^3 = 3B_4^3 \quad b_6^3 = 36B_6^3 \quad b_6^6 = 1260B_6^6.$$

These coefficients have been previously determined experimentally through standard ESR measurements on grown $\text{Gd}^{3+}:\text{Al}_2\text{O}_3$ for comparable concentrations [29, 30] at 4.2K. These parameters are used in our Hamiltonian model, with minor ($< 3\%$) adaptation of b_2^0 from +3123 to +3153 MHz for optimal fitting. The parameters used for modelling in this work are shown in Table. 1.

The Gd^{3+} substitutes into the two inequivalent Al sites of the Al_2O_3 of C_3 symmetry. Both sites share the same z-axis, but are rotated about this axis by 60° with respect

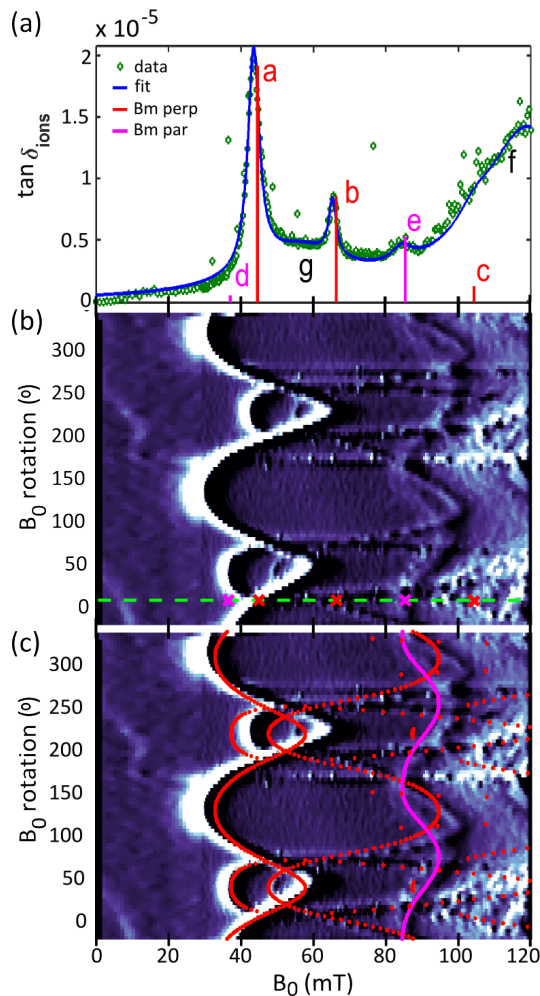


FIG. 2. (a) An individual absorption spectroscopy trace taken for B_0 rotated 5° (trace position is indicated with green dashed line in Fig. 2b). The resulting $\tan \delta_{ions}$ data is shown (green). Numerical modelling of expected ESR degeneracy points for the Gd^{3+} in Al_2O_3 spin system in perpendicular mode $B_{m,(a,b,c)} = 44, 66, 104$ mT (red) and parallel mode $B_{m,(d,e)} = 37, 85$ mT (pink) are marked with respect to relative amplitude obtained from modelling. The fitted overlay (blue) comprises the summation of $Gd^{3+}:Al_2O_3$ spin system transitions, impurities and an additional unknown transition. Parameters are detailed in Table 2. (b) The total angular dependent ESR spectra intensity plot. An edge detection filter is used to enhance weaker transitions: high contrast correspond to ESR's. (c) The angular ESR spectra with expected peak positions calculated using EASYSYPIN numerical modelling. Operation in perpendicular mode (red) and parallel mode (pink).

TABLE I. Ground state crystal field splitting parameters of $Gd^{3+}:Al_2O_3$ in MHz, used for modelling.

$b_2^0 = +3153$	$b_4^3 = 54.9$
$b_4^0 = 77.9$	$b_6^6 = 14.9$
$b_6^0 = 3.0$	$b_6^3 < 3.0$
$g = 1.9912$	

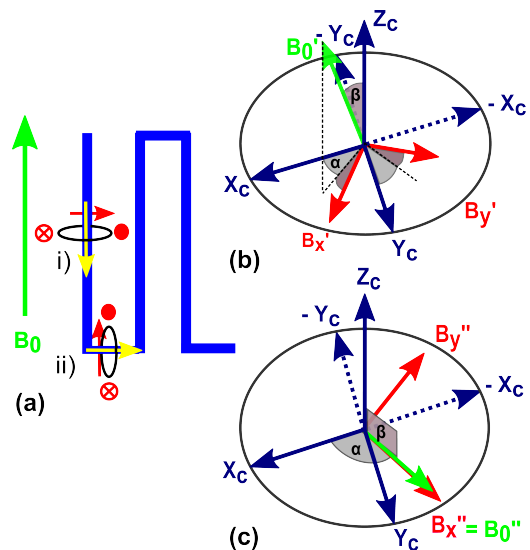


FIG. 3. (a) With B_0 (green) parallel to nominal magnetic field B_z axis the current flowing in the micro-resonator inductor is either parallel (i) or perpendicular (ii) to B_0 . We consider components of the oscillating microwave magnetic field B_{mw} (red) for each case and relative orientation to B_0 . (i) B_{mw} components are perpendicular to B_0 in all components. (ii) B_{mw} has components both perpendicular and parallel to B_0 . (b) A vector diagram depicting the transformation for case (i) of B_0 to B'_0 : where $\alpha = 30$ and $\beta = 33$, B_{mw} components are perpendicular. (c) A vector diagram depicting the transformation for case (ii) of B_0 to B''_0 : where $\alpha = 120$ and $\beta = 90$. B_{mw} components are perpendicular to B_0 in B''_y and parallel in B''_x .

to each other. The spin system also has a large zero-field splitting parameter $D = b_2^0$ attributable to the electric field produced by the O-ions surrounding the Al sites.

The experimental system is governed by the geometry of our LE device, which results in a number of configurations between our static magnetic field (B_0) and oscillating microwave field component (B_{mw}). We begin by considering the case of zero rotation, where B_0 is parallel to B_z , such that the current flowing within the micro-resonator inductor is either parallel or perpendicular to B_0 due to the LE geometry as depicted in Fig. 3a. When the direction of current flow is parallel to B_0 , the oscillating microwave magnetic field component B_{mw} is always perpendicular to B_0 (Fig. 3a(i)). Where the direction of current flow is perpendicular to B_0 , the B_{mw} component is either perpendicular or parallel to B_0 (Fig. 3a(ii)).

In order to model such a system, we must transform our static crystal frame into the laboratory frame, accounting for the R-cut crystal. We therefore consider the relative translations of B_0 from the static crystal frame $[X_c Y_c Z_c]$ into the laboratory frame assuming a start position where $B_0 = Z_c$. In the case where current flow is parallel to B_0 (Fig. 3a(i)): B_0 is brought into laboratory frame by a transformation $[\alpha \beta \gamma] = [30 \ 33 \ 0]$ as shown in Fig. 3b. The resulting B'_0 is always perpendicu-

lar to the B_{mw} component in either B'_x or B'_y . In the case where current flows perpendicular to B_0 (Fig. 3a(ii)): B_0 is brought into laboratory frame by a transformation $[\alpha \beta \gamma] = [120 \ 90 \ 0]$ as shown in Fig. 3c. The resulting B''_0 is both perpendicular and, importantly parallel to B''_{mw} components B''_y and B''_x respectively.

We numerically diagonalize our Hamiltonian for each of these operational modes for each B_0 rotation and find our model is in excellent agreement with the experimental data (Fig. 2c). We find the observed features of higher intensity within our experimental data correspond to operation where B_0 and B_{mw} components are perpendicular (red overlay in Fig. 2c). The observed features of lower intensity within our experimental data correspond to a parallel B_0 and B_{mw} (pink overlay in Fig. 2c). An example of this on a single trace is shown in Fig. 2a, where modelled ESR transitions B_m are marked: $B_{m,(a,b,c)} = 44, 66, 104$ mT (red) and $B_{m,(d,e)} = 37, 85$ mT (pink), distinguished by perpendicular and parallel mode operation respectively.

We can consider the relative areas within which the oscillating magnetic field is flowing both perpendicular and parallel to B_0 of $3400 : 832/2 \mu m^2 \approx 8.2 : 1$ and compare this to relative intensities of the ESR spectra: $8.75 : 1$, which is accurate to within 10%.

The resulting features of a single individual absorption trace can be fit with a convolution of functions where the spin ensemble and cavity are modelled as a single mode harmonic oscillator [14]:

$$Q_m = \frac{\Delta^2 + \gamma^2}{2g_c^2\gamma + \kappa(\Delta^2 + \gamma^2)}\omega_r, \quad (1)$$

where Δ is the detuning from the fitted ESR transition B_f , κ is the cavity line-width = 0.13 MHz, γ is the spin line-width and g_c the collective coupling strength. An example of such a fit is overlaid atop an individual absorption spectroscopy trace in Fig. 2a (blue).

In order to fit the data, we use the numerically modelled ESR degeneracy centre frequencies (B_m) as start points and constrain κ . We also include two additional broad ESR features in our function - the first is potentially attributable to Fe^{3+} impurities in sapphire, which when modelled provides an ESR of $B_{m,f} = 119.9$ mT. The second is an unknown background feature previously observed in literature at around 57 mT [22, 26]. For the fit shown in Fig. 2a we extract the parameters detailed in Table. 2.

It is not surprising that we do not observe the $B_{m,d} = 37$ mT transition, since the expected relative intensity of this transition at $T = 250$ mK is very low. Neglecting $B_{m,d}$, we calculate the root-mean-square deviation between each B_m and B_f across the entire ESR spectra and find an average of 3% error. We believe this to be in excellent agreement, suggesting that the ions are successfully implanted and crystal structure retained.

Notably, our modelled system is obtained using parameters modified by < 3% from measurements obtained in

TABLE II. Extracted parameters from fitting data with a convolution of Eq. 1's.

Peak	B_m (mT)	B_f (mT)	γ (MHz)	g_c (MHz)	System
a	44	43.4	53	4.5	Gd ³⁺ \perp
b	66	65.4	34	1.8	Gd ³⁺ \perp
c	104	104.3	150	2.1	Gd ³⁺ \perp
d	47	37.1	N/A	N/A	Gd ³⁺ \parallel
e	85	84.1	100	1.7	Gd ³⁺ \parallel
f	119	120.0	450	3.0	Impurities: Fe ³⁺
g	N/A	57.0	500	4.3	Unknown

grown Gd³⁺ in Al₂O₃ crystals [29]. This suggests good integration of the dopant ions into only the relevant lattice sites and that the expected system symmetries are maintained despite the high energy, near surface implantation.

In these and previous measurements of implanted rare-earth-ion-superconductor systems, coupling strengths have been limited by excessive line-widths [22, 25]. The causes of such line-width broadening can be manifold: indicative of inhomogeneous external fields, imperfections in the crystalline environment, i.e. poor site symmetry due to defects, or excessive spin-spin interactions [31].

As our experimental ESR's are in good agreement with our modelled system based on crystal field parameters of grown Gd³⁺ in Al₂O₃ at similar concentrations [29], this suggests that dispersion arising from local defects in the crystalline environment may not be the primary cause of our excessive line-width broadening. Notably, line-width broadening is not observed within flip-chip devices coupled to superconducting micro-resonator devices where the relative distances between the two systems are large [32]. Neither is broadening prevalent when coupling to other types of cavities where superconducting structures are not present [33].

Instead, one possible explanation could be that local field distortions or crystal strain induced by the close proximity of the superconductor, may be accountable for the line-width broadening. It is interesting to note that we do not observe any angular dependence in the extracted line-widths and that the Gd³⁺ parallel contributions have larger line-widths, suggesting a greater relative inhomogeneity in the oscillating magnetic field distribution due to the inductive meander turns.

It is also worth considering the impact of the resonator geometry on the resulting ESR spectra. We believe this further highlights the need for controllable local implantation techniques in order to create successful hybrid devices integrating spin ensembles and superconducting structures.

In conclusion, we demonstrate characterization of a locally implanted Gd³⁺ in Al₂O₃ system utilizing angular dependent microwave ESR spectroscopy at milli-kelvin temperatures. We find that, despite the high energy and near surface implantation, the resulting angular-

ESR spectra is in excellent agreement with the modelled Hamiltonian parametrized by symmetries obtained from a grown Gd^{3+} in Al_2O_3 system. These results support the successful integration of the dopant ions into their relevant lattice sites. We also observe clear contributions from individual microwave field components of our micro-resonator, emphasising the need for controllable local implantation when coupling spins to superconducting quantum architectures. We further demonstrate that angular-

micro-ESR spectroscopy can provide an excellent means of studying even small numbers of spins, giving valuable feedback towards developing appropriate materials for future rare-earth based quantum information technologies.

We thank, J. Molloy, Y. Andreev, V. Atuchin, A. Zoladek-Lemanczyk, D. Cox for fruitful discussions and support. This work was supported by the NMS, Swedish Research Council (VR) and Linneqs centre. Access to the IBC was supported by the EC program SPIRIT, contract no: 227012.

-
- [1] M. H. Devoret and R. J. Schoelkopf, "Superconducting circuits for quantum information: an outlook," *Science*, vol. 339, no. 6124, pp. 1169–74, 2013.
- [2] Z.-L. Xiang, S. Ashhab, J. Q. You, and F. Nori, "Hybrid quantum circuits: Superconducting circuits interacting with other quantum systems," *Rev. Mod. Phys.*, vol. 85, pp. 623–653, 2013.
- [3] B. Blinov, D. Moehring, L.-M. Duan, and C. Monroe, "Observation of entanglement between a single trapped atom and a single photon," *Nature*, vol. 428, no. 6979, pp. 153–157, 2004.
- [4] W. Rosenfeld, S. Berner, J. Volz, M. Weber, and H. Weinfurter, "Remote preparation of an atomic quantum memory," *Phys. Rev. Lett.*, vol. 98, no. 5, p. 050504, 2007.
- [5] J. Verdú, H. Zoubi, C. Koller, J. Majer, H. Ritsch, and J. Schmiedmayer, "Strong magnetic coupling of an ultracold gas to a superconducting waveguide cavity," *Phys. Rev. Lett.*, vol. 103, p. 043603, 2009.
- [6] M. Neeley, M. Ansmann, R. C. Bialczak, M. Hofheinz, N. Katz, E. Lucero, A. Oconnell, H. Wang, A. Cleland, and J. M. Martinis, "Process tomography of quantum memory in a josephson-phase qubit coupled to a two-level state," *Nat. Phys.*, vol. 4, no. 7, pp. 523–526, 2008.
- [7] A. L. Falk, B. B. Buckley, G. Calusine, W. F. Koehl, V. V. Dobrovitski, A. Politi, C. a. Zorman, P. X.-L. Feng, and D. D. Awschalom, "Polytype control of spin qubits in silicon carbide," *Nat. Commun.*, vol. 4, p. 1819, 2013.
- [8] A. André, D. DeMille, J. M. Doyle, M. D. Lukin, S. E. Maxwell, P. Rabl, R. J. Schoelkopf, and P. Zoller, "A coherent all-electrical interface between polar molecules and mesoscopic superconducting resonators," *Nat. Phys.*, vol. 2, no. 9, pp. 636–642, 2006.
- [9] P. Rabl, D. DeMille, J. Doyle, M. Lukin, R. Schoelkopf, and P. Zoller, "Hybrid quantum processors: Molecular ensembles as quantum memory for solid state circuits," *Phys. Rev. Lett.*, vol. 97, no. 3, p. 033003, 2006.
- [10] M. Steger, K. Saeedi, M. L. W. Thewalt, J. J. L. Morton, H. Riemann, N. V. Abrosimov, P. Becker, and H.-J. Pohl, "Quantum information storage for over 180 s using donor spins in a ^{28}Si semiconductor vacuum," *Science*, vol. 336, no. 6086, pp. 1280–3, 2012.
- [11] J. Twamley and S. D. Barrett, "Superconducting cavity bus for single nitrogen-vacancy defect centers in diamond," *Phys. Rev. B*, vol. 81, p. 241202, 2010.
- [12] A. Imamolu, "Cavity qed based on collective magnetic dipole coupling: Spin ensembles as hybrid two-level systems," *Phys. Rev. Lett.*, vol. 102, no. 8, p. 083602, 2009.
- [13] J. Wesenberg, A. Ardavan, G. Briggs, J. Morton, R. Schoelkopf, D. Schuster, and K. Mølmer, "Quantum Computing with an Electron Spin Ensemble," *Phys. Rev. Lett.*, vol. 103, no. 7, p. 070502, 2009.
- [14] D. I. Schuster, a. P. Sears, E. Ginossar, L. DiCarlo, L. Frunzio, J. J. L. Morton, H. Wu, G. a. D. Briggs, B. B. Buckley, D. D. Awschalom, and R. J. e. a. Schoelkopf, "High-cooperativity coupling of electron-spin ensembles to superconducting cavities," *Phys. Rev. Lett.*, vol. 105, no. 14, p. 140501, 2010.
- [15] C. Grezes, B. Julsgaard, Y. Kubo, M. Stern, T. Umeda, J. Isoya, H. Sumiya, H. Abe, S. Onoda, T. Ohshima, V. Jacques, J. Esteve, D. Vion, D. Esteve, K. Mølmer, and P. Bertet, "Multimode storage and retrieval of microwave fields in a spin ensemble," *Phys. Rev. X*, vol. 4, p. 021049, 2014.
- [16] Y. Kubo, C. Grezes, a. Dewes, T. Umeda, J. Isoya, H. Sumiya, N. Morishita, H. Abe, S. Onoda, T. Ohshima, V. Jacques, a. Dréau, J.-F. Roch, I. Diniz, a. Auffeves, D. Vion, D. Esteve, and P. Bertet, "Hybrid quantum circuit with a superconducting qubit coupled to a spin ensemble," *Phys. Rev. Lett.*, vol. 107, no. 22, p. 220501, 2011.
- [17] S. Probst, H. Rotzinger, A. V. Ustinov, and P. A. Bushnev, "Microwave multimode memory with an erbium spin ensemble," *Phys. Rev. B*, vol. 92, no. 1, p. 014421, 2015.
- [18] A. Bienfait, J. J. Pla, Y. Kubo, M. Stern, X. Zhou, C. C. Lo, C. D. Weis, T. Schenkel, M. L. W. Thewalt, D. Vion, D. Esteve, B. Julsgaard, K. Moelmer, J. J. L. Morton, and P. Bertet, "Reaching the quantum limit of sensitivity in electron spin resonance," *arXiv*, 2015.
- [19] S. Probst, H. Rotzinger, A. V. Ustinov, and P. A. Bushnev, "Microwave multimode memory with an erbium spin ensemble," *Phys. Rev. B*, vol. 92, p. 014421, 2015.
- [20] C. Thiela, T. Böttgerb, and R. Conea, "Rare-earth-doped materials for applications in quantum information storage and signal processing," *J. Lumin.*, vol. 131, pp. 353–361, 2011.
- [21] C. O'Brien, N. Lauk, S. Blum, G. Morigi, and M. Fleischhauer, "Interfacing superconducting qubits and telecom photons via a rare-earth-doped crystal," *Phys. Rev. Lett.*, vol. 113, p. 063603, 2014.
- [22] I. Wisby, S. E. de Graaf, R. Gwilliam, a. Adamyan, S. E. Kubatkin, P. J. Meeson, a. Y. Tzalenchuk, and T. Lindström, "Coupling of a locally implanted rare-earth ion ensemble to a superconducting micro-resonator," *App. Phys. Lett.*, vol. 105, no. 10, p. 102601, 2014.
- [23] D. M. Toyli, C. D. Weis, G. D. Fuchs, T. Schenkel, and

- D. D. Awschalom, “Chip-scale nanofabrication of single spins and spin arrays in diamond,” *Nano. Lett.*, vol. 10, no. 8, pp. 3168–3172, 2010.
- [24] N. Kukharchyk, S. Pal, J. Rödiger, A. Ludwig, S. Probst, A. V. Ustinov, P. Bushev, and A. D. Wieck, “Photoluminescence of focused ion beam implanted $\text{er}^{3+}:\text{y}_2\text{si}_2\text{o}_7$ crystals,” *Phys. Status Solidi RRL*, vol. 8, no. 10, pp. 880–884, 2014.
- [25] S. Probst, N. Kukharchyk, H. Rotzinger, A. Tkalčec, a. D. Wieck, M. Siegel, a. V. Ustinov, P. a. Bushev, a. Tkalčec, and S. Wünsch, “Hybrid quantum circuit with implanted erbium ions,” *App. Phys. Lett.*, vol. 105, no. 16, p. 162404, 2014.
- [26] W. G. Farr, D. L. Creedon, M. Goryachev, K. Benmessai, and M. E. Tobar, “Ultrasensitive microwave spectroscopy of paramagnetic impurities in sapphire crystals at millikelvin temperatures,” *Phys. Rev. B*, vol. 88, no. 22, p. 224426, 2013.
- [27] H. Toida, Y. Matsuzaki, K. Kakuyanagi, X. Zhu, W. J. Munro, K. Nemoto, H. Yamaguchi, and S. Saito, “Electron paramagnetic resonance spectroscopy using a dc-squid magnetometer directly coupled to an electron spin ensemble,” *arXiv*, p. 9, 2015.
- [28] S. Stoll and A. Schweiger, “Easypin, a comprehensive software package for spectral simulation and analysis in epr.,” *J. Magn. Reson.*, vol. 178, no. 1, pp. 42–55, 2006.
- [29] S. Geschwind and J. P. Remeika, “Paramagnetic resonance of gd^{3+} in al_2o_3 ,” *Physical Review*, vol. 122, no. 3, p. 757, 1961.
- [30] P. H. E. Meijer and J. Lewiner, “Energy levels, wave functions, dipole and quadrupole transitions of trivalent gadolinium ions in sapphire,” *Journal of Research of the National Bureau of Standards*, vol. 75A, no. 5, pp. 493–533, 1971.
- [31] A. Abragam and B. Bleaney, *Electron Paramagnetic Resonance of Transition Ions*. Oxford University Press, 1970.
- [32] A. Tkalčec, S. Probst, D. Rieger, H. Rotzinger, S. Wünsch, N. Kukharchyk, A. D. Wieck, M. Siegel, A. V. Ustinov, and P. Bushev, “Strong coupling of an er^{3+} doped $\text{y}_2\text{si}_2\text{o}_7$ crystal to a superconducting resonator,” *Phys. Rev. B*, vol. 90, p. 075112, 2014.
- [33] S. Probst, A. Tkalčec, H. Rotzinger, D. Rieger, J.-M. Le Floch, M. Goryachev, M. E. Tobar, A. V. Ustinov, and P. A. Bushev, “Three-dimensional cavity quantum electrodynamics with a rare-earth spin ensemble,” *Physical Review B*, vol. 90, p. 100404, 2014.